



Citation for published version:

Meliza, CD, Kostuk, M, Huang, H, Nogaret, A, Margoliash, D & Abarbanel, HDI 2014, 'Estimating parameters and predicting membrane voltages with conductance-based neuron models', *Biological Cybernetics*, vol. 108, no. 4, pp. 495-516. <https://doi.org/10.1007/s00422-014-0615-5>

DOI:

[10.1007/s00422-014-0615-5](https://doi.org/10.1007/s00422-014-0615-5)

Publication date:

2014

Document Version

Early version, also known as pre-print

[Link to publication](#)

This is a pre-print version of an article published in *Biological Cybernetics*. The final authenticated version is available online at: <https://doi.org/10.1007/s00422-014-0615-5>

University of Bath

Alternative formats

If you require this document in an alternative format, please contact:
openaccess@bath.ac.uk

General rights

Copyright and moral rights for the publications made accessible in the public portal are retained by the authors and/or other copyright owners and it is a condition of accessing publications that users recognise and abide by the legal requirements associated with these rights.

Take down policy

If you believe that this document breaches copyright please contact us providing details, and we will remove access to the work immediately and investigate your claim.

Estimating Parameters and Predicting Membrane Voltages with Conductance-Based Neuron Models

C Daniel Meliza^{1,*}, Mark Kostuk², Hao Huang¹, Alain Nogaret³, Daniel Margoliash¹, Henry D. I. Abarbanel⁴

1 Department of Organismal Biology and Anatomy, University of Chicago, Chicago, Illinois, USA

2 Department of Physics, University of California San Diego, La Jolla, California, USA

3 Department of Physics, University of Bath, Claverton Down, Bath, UK

4 Department of Physics and Marine Physical Laboratory (Scripps Institution of Oceanography), Bio Circuits Institute, University of California San Diego, La Jolla, California, USA

* E-mail: dmeliza@uchicago.edu

Abstract

Recent results demonstrate techniques for fully quantitative, statistical inference of the dynamics of individual neurons described by multiple voltage-gated channels in a Hodgkin-Huxley framework. These approaches have been successfully applied to simulated data from model neurons. Here we apply an method based on a variational principle to whole-cell recordings from a population of real neurons recorded in a slice preparation of the zebra finch forebrain nucleus HVC. Our results demonstrate that using only 1500 ms of voltage recorded while injecting a complex current waveform, we can estimate the values of 12 state variables and 73 parameters in a dynamical model, such that the model accurately predicts the responses of the neuron to novel injected currents. A less complex model produced consistently worse predictions, indicating that the additional currents contribute significantly to the dynamics of these neurons. Preliminary results indicate some differences in the physiological properties of the models for different classes of HVC neurons, which accords with expectations from the biology. Whereas the model for each cell is incomplete (representing only the somatic compartment, and likely to be missing classes of channels that the real neurons possess), our approach opens the possibility to investigate in modeling the plausibility of additional candidate classes of channels that the cell might possess, thus improving the models over time. These results provide an important foundational basis for building biologically realistic network models, such as the one in HVC that is central to the process of developmental vocal learning in songbirds.

Author Summary

The relationship between a neuron's inputs and outputs is key to understanding how circuits of neurons perform the computations underlying complex animal behaviors. Many efforts to understand this relationship mechanistically make use of extensions of the canonical model developed by Hodgkin and Huxley. These models are biologically realistic and can predict the behaviors of neurons in numerous systems, but contain many unknown parameters and state variables that have been difficult to measure experimentally. We recently developed a method to infer these values for individual neurons from their responses to a sufficiently complex current input. We applied this method to neurons in the zebra finch song system, and found that for most neurons we could estimate values for the model from less than 2 s of data. Models incorporating such estimated parameters were then able to accurately predict the responses of the neurons to novel patterns of stimulation. Our results demonstrate a tool for studying circuits of diverse kinds of neurons. These methods can be applied to many dynamical systems where there is limited or noisy data.


Introduction

Circuits of neurons typically comprise multiple cell types with distinct anatomical and physiological properties. Behaviors of circuits and organisms depend both on the intrinsic properties of component neurons and on the dynamics of their interactions. Many models for the emergence of complex behaviors in neurons and circuits are based on the formalism proposed by Hodgkin and Huxley [1], which represents membrane dynamics in terms of ion currents through passive, voltage-gated, and ligand-gated conductances. The dynamics of these conductances can in turn be explained by biophysical properties of the specific ion channels expressed by the cell. These models can thus provide mechanistic insights into the relationship between generally specified cell properties and the emergence of complex behaviors [2–5].

Although the tools for developing conductance-based models have matured in recent decades [6–8], a significant impediment to wider use is the large number of free parameters in realistic models that include multiple compartments, moderate numbers of currents, or networks of synaptic connectivity. Although many parameters can be constrained by detailed anatomical reconstructions and experimental data on biophysics, others need to be determined for neurons individually. There is growing evidence of substantial heterogeneity among neurons with similar morphology and physiology. Even though many kinds of ion channels have been identified and characterized [9, 10], their expression, spatial distribution, isoform composition, and phosphorylation states may vary

widely among cells [11, 12] and over time [13, 14]. Furthermore, because of nonlinear relationships between channel kinetic parameters and observable behavior, experimental data on average values for these parameters within a population do not constrain well the values for individual neurons [15, 16].

There have been numerous efforts to develop automated methods to directly estimate the parameters that reproduce observed biological data from individual neurons [17, 18]. Approaches range from ~~brute-force~~ grid, stochastic, and evolutionary search algorithms [19–24] to statistical inference based on probabilistic frameworks that explicitly account for errors in measurement and model specification [25–28]. These methods have been successful in estimating maximal conductances, which is a linear problem, but channel kinetic parameters have proven more challenging, as this is a nonlinear ~~task~~ [29, 30].

We have previously described an exact statistical formalism for the problem of estimating the unknown states and parameters of conductance-based neuronal models given measurements of the membrane potential alone [31–33]. Using here an approximation to the exact formulation [31], we apply the method to whole-cell recordings in slices of the song premotor area HVC (a proper name) from zebra finches (*Taniopygia gutatta*). HVC comprises three broadly defined categories of neurons [34]: those projecting exclusively to striatal neurons in area X, those projecting exclusively to the motor ~~output~~ nucleus RA, and interneurons whose axons are confined to HVC. Each of these categories encompasses at least two subtypes [35–38], and there are likely to be more categories and subclasses of HVC neurons. Intracellular recordings *in vivo* and in a slice preparation have defined principal attributes of the HVC circuit [39, 40], but the connectivity and intrinsic membrane properties of HVC neurons that give rise to the precisely timed patterns of activity that HVC emits during production of song [41] remain an active area of research [42–44] 

Our goals were to test whether the methods developed in [31–33] on simulated data also work with real neurons and if so, to determine whether the models give insight into the biology of HVC. Because the models are only an approximation to the physical system, and the true channel complements and kinetic properties are not known, we test the models by generating predictions to novel current injections and cross-validating against recorded responses. We find that with a sufficiently complex model we can generate predictions for most neurons in HVC that are nearly as good as the intrinsic variability of the neurons.

Results

Estimation and prediction of HVC neuron responses to injected current

We made whole-cell recordings from 26 HVC neurons and stimulated them in current-clamp by injection of a complex current waveform designed to close and open a broad range of voltage-gated ion channels. The observed voltage and the known injected current from 1500 ms of the recording were used to estimate the unknown states and parameters of conductance-based dynamical models for each neuron. The completed model was then integrated forward to ~~to~~ predict the response of the neuron to the remainder of the recording epoch.

Because the full complement of channels expressed by HVC neurons is not known, the model was developed iteratively, starting with a relatively simple model used in an earlier theoretical study [31]. The initial model contained a transient sodium current (NaT), a non-inactivating potassium current (K1), a hyperpolarization-activated cation current (HCN), and a passive leak current. Using a set of neurons that exemplified the range of physiological responses we observed, we compared the predictions of the models to the recorded voltages, and added additional voltage-gated currents that might account for features of the response missing from the prediction. Although calcium- and sodium-gated currents may be present in some classes of HVC neurons [45], their dynamics are complex and difficult to infer from limited amounts of data, so they were not explored in this analysis. The predictions in each iteration were evaluated using spike shape, spike rate, and the RMS deviation in the subthreshold voltage. The final model included a persistent sodium current (NaP), an inactivating potassium current (K2), a slow non-inactivating potassium current (K3), a high-threshold L-type calcium current (CaL), and a low-threshold T-type calcium current (CaT), with a total of 12 state variables and 72 free parameters. ~~These currents do not represent specific, genetically identified ion channels but rather a composite of ion channels with the same gating kinetics.~~

We highlight three example neurons. Two of the neurons, which showed little or no adaptation to step currents, were likely to be X-projecting (hereafter, N1 and N2) (Figures 1C and 2C). The third, which showed rapid adaptation to step currents, was likely to be RA-projecting (N3) (Figure 3C). The measured voltage trace and injected current used to complete the neuron model for each of the exemplar neurons is shown in Figures 1A, 2A, and 3A. The recorded voltage trace is shown in black and the final estimated $V_m(t)$ of the model is in cyan. The magenta traces show the results of integrating the completed model forward using the estimated values of the parameters and state variables at the end of the assimilation window and the known injected current.

To further validate the model, a prediction for a different recording epoch was created, using a short (100 ms)

assimilation window to estimate only the unobserved state variables (giving us the initial condition of the channel gating particles), while the previously obtained parameters were held fixed. This model was then integrated forward with the known injected current to predict the response to the rest of the epoch (Figures 1B, 2B, and 3B). One additional parameter I_{dc} was optimized for the prediction, which compensated for drifts in recording quality and membrane potential over the time between the parameter assimilation epoch and the inter-epoch prediction.

For both the intra- and inter-epoch predictions, the predicted responses reasonably matched the recordings in terms of spike rate, spike timing (see tick marks in Figures 1–3) and subthreshold voltage. The predicted spike times did not always align perfectly with spikes in the data, but the variability was comparable to what we observed in measured responses to the same stimuli presented at different times (data not shown). Similarly, errors in the predicted responses to hyperpolarizing currents were consistent with small variations in input resistance over the time course of the recording. Predicted spikes from the models closely matched the shape of the spikes in the recordings (Figures 1D, 2D, and 3D), with the exception of a “kink” visible in the phase plane plots of the spikes for N1 and N2 (Figures 1E and 2E).

We also compared responses to step currents with predicted responses of the model neurons (Figures 1C, 2C, and 3C). The models accurately predicted many of the features of these responses (for example, the initial overshoot in depolarization in Figure 3C), but on the whole the predictions were not as good as for the complex currents.

Estimated currents and channel kinetics

A detailed view of the estimated currents and gating state variables during the data assimilation window is shown for neurons N1, N2, and N3 in Figures 4, 5, and 6 respectively. As expected, the neurons showed a strong dependence upon the fast sodium current and a potassium current for spike generation, but subtle differences in the strength and kinetics of these currents led to differences in spike shape and excitability. Compared to N2, N1 (Figure 4) had a higher spike rate, a stronger after-hyperpolarization potential (AHP), and little to no change in spike shape or rate with prolonged depolarization (i.e., adaptation). In the model, these differences were due to a relatively stronger potassium current in N1, which repolarized the cell more rapidly and strongly. In the model for N2 (Figure 5), the K current was weaker and somewhat slower, leading to a weaker AHP but also to a buildup of NaT inactivation, which may account for changes in spike shape and rate over sustained depolarization.

As with N1, the model for N3 (Figure 6) had a strong K current that resulted in a pronounced AHP. However, this current was supplied by a channel with m^1 kinetics, which caused it to stay open during prolonged depolarizations. This current was balanced by a positive current from the persistent sodium channel. Together, these currents

provided strong shunting inhibition that prevented the model from firing more than one action potential and gave it its phasic response properties.

The relative importance of each of the currents in the model was ascertained in two ways. The first was to compare the maximal conductances, both directly (Table S1) and as a fraction of the total membrane conductance ($\tilde{g}_\alpha = g_\alpha / \sum_i g_i$, Figure 7A, dark bars). As noted above, the N2 model had strong NaT conductance and relatively weak K conductances, accounting for its rapid depolarization (Figure 2E) and weak AHP. For N3 the dominant potassium conductance was from K3.

Categorizing neurons based upon their channel maximal conductances g_α may not accurately reflect the dynamical importance of the channels in driving the membrane voltage over a significant time interval. It is not the maximal conductance, but the strength of the current that influences changes in the membrane voltage. For example, large currents may result from small conductances for a channel with a very slow time constant. The second method we used to identify important currents was to calculate the fraction of the total current from each channel type α , $\tilde{I}_\alpha = \left\langle \frac{|I_\alpha|}{\sum_i |I_i|} \right\rangle_T$. These values are shown by the light bars in Figure 7A. The absolute value was used so that the comparison was relative to the magnitude of the total current flux, and the time average was taken over the data assimilation window, T . Comparing \tilde{I} values across neurons reveals the contribution of NaP to N3 dynamics, CaT to N2 dynamics, and K3 to the dynamics of all three neurons, effects that are not seen in the maximal conductances because these channels were weakly but tonically active. Conversely, the NaT currents were strongly expressed in terms of \tilde{g} , but their rapid opening and closing resulted in a diminished contribution to the total neuronal current. The differences in \tilde{I}_{Na} between the three exemplar neurons appears to correspond to the differences in the number of action potentials produced during the assimilation window.

Additional differences between neurons were also seen in the parameters governing channel dynamics. Figure 7B shows the equilibrium state ($x_\infty(V)$) and relaxation time constant ($\tau(V)$) as a function of voltage for the activation and inactivation variables for several channels. The K3 channel in the model for N3 had a higher $V_{1/2}$ relative to both the same channel in the other neurons and relative to the $V_{1/2}$ of the K2 channels in the N1 and N2 models (Figure 7B). This feature allowed some proportion of the K3 channels to remain open in moderately depolarized conditions, possibly contributing to the phasic response properties of this neuron. Also for N3, the $V_{1/2}$ for NaT inactivation occurred at lower voltages relative to the other two neurons, which gave the model relatively slow inactivation kinetics at hyperpolarized potentials, and led to a buildup of inactivation that may have contributed to this neuron's phasic responses.

Posterior distribution of parameter estimates

The parameter and state estimates obtained through the variational method are point estimates representing the values most likely to give rise to the data. To explore the posterior variance (i.e., uncertainty) of these estimates, we generated sampling distributions using a Metropolis-Hastings Monte Carlo algorithm (see Materials and Methods and [32]). The marginal posterior distributions of selected parameters from the three exemplar neurons are shown in Figure 8. Some parameters were strongly constrained by the data, such that only a narrow range of values was consistent with the observed response, whereas other parameters had broader distributions. Several of the parameters had complex, multimodal distributions. Note that the graphs only show marginal distributions, and cannot represent manifolds in the parameter space where certain combinations of parameter values are particularly probable or not.

Model validation and selection

After the exemplar neurons were characterized, the final form of the model was used in data assimilation for all 26 neurons in the recorded population. For each neuron, three recording epochs with different stimulation waveforms were chosen. The stimulation protocols were similar across neurons except in amplitude, which had been adjusted during the experiment to ensure sufficient numbers of action potentials. Each completed model was used to generate an intra-epoch prediction (as in Figure 1A), which was compared to the data using metrics for subthreshold voltage, spike rate, spike shape, spike timing, and total correlation (see Materials and Methods).

There was substantial variability within neurons in prediction quality. Often, models estimated from different epochs reproduced different features of the response better than others. Therefore, for each neuron we picked the model that gave the best overall performance across all the prediction metrics. Table 1 shows summary statistics of the prediction metrics for all the models and for the best-ranked models for each neuron. It also shows summary statistics for the same metrics applied to recorded responses to the same stimulus, as a measure of intrinsic variability. As quantified by these metrics, the differences between model predictions and neural responses are comparable to differences between neural responses to the same injected current. In some cases the intrinsic deviance was higher than the model deviance, although this is likely to reflect small, slow changes in input resistance over the course of the recording.

One possible explanation for high within-neuron variability in model quality is that different stimuli explored different regions of the model state space, leading to solutions that emphasized some features more than others.

We made a more extensive analysis of prediction quality using many sets of data from the three exemplar neurons. For each neuron, we selected 26–28 recording epochs, and from each epoch between 1–3 (mean 2.6) overlapping segments of data to assimilate. Predictions for each completed model were compared to the data, and the variance in prediction quality between epochs was compared to the variance within epochs. For three of the five metrics, between-epoch variance was significantly higher than within-epoch variance (F-test; spike shape: $F_{39,152} = 2.85$, $P = 2.7 \times 10^{-6}$; spike timing: $F_{41,163} = 3.36$, $P = 2.4 \times 10^{-8}$; correlation: $F_{41,163} = 1.50$, $P = 0.041$; spike rate: $F_{41,163} = 1.46$, $P = 0.05$; subthreshold deviance: $F_{41,163} = 1.14$, $P = 0.28$), suggesting that differences in current stimulus had an effect on model quality.

To determine whether the additional currents in the model quantitatively improved predictions, the assimilation and prediction procedures were also applied to the same data using the initial model, which had only three voltage-gated conductances. By all measures, the more complex model produced better predictions. In a pairwise comparison between simple and complex models estimated from the same data, the median difference in subthreshold deviance was 1.46 mV (paired Wilcoxon test: $P = 2.7 \times 10^{-5}$), in spike rate deviance, 0.14 ($P = 5.8 \times 10^{-5}$), in spike shape deviance, 0.015 ($P = 2.6 \times 10^{-4}$), in spike coincidence, 0.11 ($P = 3.2 \times 10^{-5}$), and in correlation coefficient, 0.036 ($P = 3.7 \times 10^{-5}$). Similarly, the best-ranked complex models outperformed the best-ranked simple models (Figure 9) on all the metrics except spike timing. For 21/26 neurons (81%), the complex model produced the best overall prediction. Four of the neurons better predicted by the simpler model were putatively RA-projecting, and one was a putative interneuron.

Comparison of parameter estimates across cell types

We obtained a large enough sample of putative X-projecting ($n = 7$) and RA-projecting neurons ($n = 16$) to compare parameter estimates within and between these cell types. We selected the best model for each neuron and compared parameter estimates across the population. For the neurons better fit by the simpler model, the conductances of the omitted channels were assumed to be zero. Some parameter values were consistent across the population, some differed significantly between putative cell types, and others were highly variable without any obvious correlation to physiology. As shown in Figure 10A, relative maximal conductances for the HCN, CaT, and CaL currents were low for all the neurons. A weak contribution from the HCN current is consistent with the lack of an obvious sag current in responses to hyperpolarization (see Discussion).

For the subset of neurons identified as RA-projecting based upon their phasic response properties, relative NaT conductance was significantly lower than in putative X-projecting neurons (Wilcoxon test, $P = 0.006$). This

difference may correspond to the relatively higher excitability of X-projecting neurons. As noted above, maximal conductances do not fully reflect the dynamical importance of a current over time, but may indicate structural differences between neurons related to channel expression levels. Within each of the putatively classified groups of neurons there was substantial variability in conductance levels.

Kinetic parameter estimates also varied substantially across neurons, and we were unable to discern any obvious clustering that might correspond to specific cell types. As an example, estimates for the kinetic parameters that define the transient sodium channel are shown in Figure 10B. The activation and inactivation variables are each governed by four parameters: the half-potential $V_{1/2}$ and slope κ of the equilibrium activation $x_\infty(V)$, and the width σ and peak height τ_{max} of the relaxation time constant $\tau(V)$. Most of the estimates for the parameters associated with $x_\infty(V)$ were well within the bounds specified in the assimilation procedure, suggesting that these parameters are well constrained by the data; in contrast, many of the estimates for the parameters associated with $\tau(V)$ were at or near the bounds. It may be difficult to reliably estimate time constants from current-clamp data because the neuron does not stay at highly depolarized voltages for very long.

Discussion

These results demonstrate the application of a statistical method for estimating unknown states and parameters of complex, conductance-based, dynamical models. Using this method, which is a variational **approximation** to the high-dimensional path integral relating measured voltage to the internal dynamics of voltage-gated ion channels [31, 33], we obtained state and parameter estimates for models of individual neurons from a diverse population in the songbird vocal nucleus HVC. We used the completed models to predict responses to novel injected currents and cross-validated the predictions against the recorded responses to those stimuli. Using a broad range of metrics that emphasized different features of the response, we found that prediction errors were comparable to intrinsic variation in the neurons' responses, indicating that the models' behaviors closely matched those of the neurons at multiple levels of detail.

We began with a simple model containing only ~~three~~ voltage-gated currents, and found that additional sodium, calcium, and potassium currents were necessary to obtain good predictions for over 80% of the neurons. The better performance of the more complex model was not a consequence of overfitting a larger number of free parameters, because the models were cross-validated on data that was not used in fitting. With the full complement of currents, the model had 11 unmeasured state variables and 72 unknown parameters. To our knowledge, this is the largest

search space explored to date for conductance-based neuron models. The data assimilation method we employ here is a significant advance because it can efficiently estimate models of a size and complexity commensurate with the biophysics of real neurons.

The better performance of the more complex model also indicates, unsurprisingly, that the dynamics of most HVC neurons depend on more than the fast sodium and potassium currents that generate action potentials. Indeed, the differences in predicted spike shapes between the simpler and more complex model were relatively small compared to other features of the response like spike rate and timing. Many of the additional currents in the complex model had relatively low maximal conductances, but were responsible for a substantial fraction of the current flux (Figure 7). These currents had slower time constants, were more tonically active, and functioned in the model to modulate the cell's excitability. It is important to note that we did not enforce this behavior *a priori*: the bounds for parameters governing gating time constants usually spanned several orders of magnitude (see Table S1). Instead, the slower, more modulatory nature of the additional currents emerged from the data assimilation.

Some of the currents were consistently estimated to have low maximal conductances and relative current contributions (Figure 10), including the high-threshold calcium channel (CaL) and the hyperpolarization-activated cation channel (HCN). Therefore, it may be possible to remove them from the model formulation without substantially impacting the behavior. On the other hand, the estimated contribution may be low because the injected currents failed to activate these channels sufficiently to affect the neuron's response. In particular, HCN is a fairly slow current and may require longer and stronger hyperpolarization [37, 45].

An important consideration in modeling studies is uncertainty in parameter estimates [16, 46, 47]. Because of measurement errors, and because the model is always an approximation of the physical system, it can never perfectly reproduce the system's behavior. For a dynamical system, the distribution of parameter values that are consistent with the data is given by a high-dimensional path integral [31, 33]. The variational method gives a maximum likelihood estimate of the best parameters with the assumption of no model error. To incorporate model error, we sampled numerically from the path integral distribution [32], and found that many of the key parameters were well-constrained by the data and significantly different between neurons (Figure 8). However, most of the parameter estimates for different neurons and even different epochs from the same neuron exhibited a large degree of variance, in spite of producing similar quality predictions.

We propose several hypotheses for this variability. One, the relatively short length of the data assimilation window may mean that the current stimulation protocols insufficiently explored the state space of the model. Models estimated from different segments of data may emphasize some features of the response more than others. In

support of this hypothesis, the stimulation currents we used in data assimilation did not include long step depolarizations, and in general the models were not as good at predicting responses to step currents (e.g., Figure 1C). Furthermore, in a subset of the data, we observed significantly more variability in model quality among epochs with different current protocols than among different segments of data from the same epoch. By incorporating more data with a more diverse set of injected current stimuli for assimilation, the number of solutions should shrink, although ~~additional work is needed to deal with the computer memory requirements of larger datasets.~~

Two, because the system is nonlinear and the model is an approximation, the parameter landscape may have many local minima. Because the variational method is based on gradient descent, it is sensitive to starting conditions [cite?] and may converge on **widely divergent solutions**. Consistent with this hypothesis, studies with more global optimization strategies have found that most simple models have multiple solutions widely separated in the parameter space [15, 16, 46, 48]. Expanding the model to include a larger assortment of potential currents, such as from calcium- or sodium-dependent channels [45], ~~should~~ ameliorate this problem by expanding the parameter space to include values closer to ~~the~~ true solution. Additional compartments may also allow more global minima to be found. For example, the kink observed in the phase plot of some spikes (Figure 1C) is thought to correspond to spike generation in the initial segment of the axon [49], where sodium channel densities are often much higher than in the soma. The model used here included only one compartment for simplicity, but as a result the solutions represent a non-optimal average of the two compartments.

Finally, there are likely to be degeneracies in the actual physical system such that neurons can achieve the same physiological output with **widely divergent** parameters [11, 50–53]. The parameter variance we observed may, at least to some extent, reflect the heterogeneity of the population, even within morphologically and physiologically defined cell types. However, if this is the case, ~~the~~ solution for a given neuron will be only one of many it could adopt, and additional data from online pharmacological [45, 53] or ~~dynamic clamp manipulations~~ [54] will be needed to constrain the solution.

Diversity of cell types is a common feature of neural circuits and is likely to be functionally significant. In recent studies, conductance-based models have been less successful than more phenomenological models in predicting the responses of individual neurons [55,56], and thus have been less suitable for addressing diverse circuits in spite of the potential mechanistic insight such models provide. These results indicate that more complex, realistic conductance models can predict spike timing on par with the best phenomenological models [57,58], in addition to reproducing many fine details of the neural response that the other models cannot represent. In light of the large uncertainties in parameter estimates from these still highly simplified models, it would be premature to make strong

inferences about many of the underlying biophysical properties of the neurons under study. However, the method we describe here provides a means of efficiently characterizing individual neurons with more biologically realistic models. Such models can incorporate prior information about anatomy and channel expression and can be used to generate testable hypotheses about the roles of specific currents in the generation of complex behaviors.

Materials and Methods

Ethics Statement

All animal procedures were performed according to protocols approved by the University of Chicago Institutional Animal Use and Care Committee and consistent with the guidelines of the National Institutes of Health.

HVC Slice Preparation

Slices were prepared from adult (> 90 days post hatch) male zebra finches. Birds were deeply anesthetized with isoflurane and decapitated, and the brains were placed in ice-cold, oxygenated dissection buffer containing (in mM): 205 sucrose, 3 KCl, 1 NaH₂PO₄H₂O, 26 NaHCO₃, 25 D-glucose, 6 MgSO₄, and 0.5 CaCl (290–310 mOsm). Parasagittal slices were cut (400 μm thick, Vibratome 1000) from both hemispheres and placed in 37 °C oxygenated artificial cerebrospinal fluid (ACSF) containing (in mM): 123 NaCl, 3 KCl, 1 NaH₂PO₄H₂O, 26 NaHCO₃, 25 D-glucose, 3 MgSO₄, 1 CaCl (290–310 mOsm, pH 7.2–7.3). Slices were allowed to recover for at least 1 h, during which time the ACSF was allowed to return to room temperature. For recording, slices were superfused (1.5–2.0 mL/min) with oxygenated ACSF (23–26 °C).

Electrophysiology

Current-clamp somatic whole-cell recordings were made from 45 neurons in HVC with an NPI SEC-05L amplifier (npi electronic, Tamm, Germany). Of these, 26 neurons had spikes with peaks > 0 mV and stable resting potential < –60 mV, and were deemed suitable for analysis. Neurons were putatively classified as RA-projecting ($n = 16$) if they showed strong adaptation, firing only a single spike or a short burst at the beginning of depolarization, and X-projecting ($n = 7$) if they showed weak or no adaptation. One cell was classified as an interneuron based on its high firing rate and complete lack of adaptation, and two neurons could not be classified based on these criteria.

Cells were selected visually with differential IR optics for health but not for somatic size or shape. Patch

pipettes (3–5 M Ω) were pulled from standard-walled borosilicate glass (Model G150F-4, Warner Instruments, Hamden CT) with a Sutter P-97 (Sutter Instruments, Novato CA) and filled with internal solution containing (in mM): 130 K-gluconate, 10 Na-gluconate, 10 HEPES, 4 NaCl, 4 MgATP, 0.3 NaGTP, 10 Na-phosphocreatine, 0.1 EGTA (290–310 mOsm, pH 7.2–7.3). In some experiments 0.50% neurobiotin (Vector Labs, Burlingame CA) was added to the internal solution. Pipette capacitance and series resistance were compensated on the amplifier. Voltage and injected current (as reported by the amplifier) were high-pass filtered at 20 kHz and digitized at 50 kHz with a PCI-6052E (National Instruments, Austin TX). Injected currents consisted of positive and negative steps of varying amplitude and a complex, non-sinusoidal waveform derived from the Lorenz equations (e.g., Figure 1A) delivered at varying frequencies. The amplitude of the complex current was set to ensure that spikes were elicited and the neuron was hyperpolarized to at least -90 mV for some period of time. Data collection was controlled by custom software written in MATLAB (The Mathworks, Natick MA).

Dynamical State and Parameter Estimation of Neuron Models

Data assimilation is the general name given to the incorporation of information from measurements of a physical system into a set of model dynamical equations with the goal of finding a set of parameters and state variables such that the model best describes the data. We call a model with parameters estimated in this manner a completed model. In this preparation, the data to be assimilated were the measurements of membrane potential from the somatic current-clamp electrode, which was also used to deliver selected forcing by current injection. The same principles apply to preparations in which data from other parts of the cell are **be** available from other electrodes or fluorescent reporters [59].

Statistical properties of estimated quantities such as the expected state during a learning window, or in a prediction window following the learning period, along with the estimated errors of these expected values, are given by the evaluation of a path integral through the state space of the model [60–63]. The appropriate integrals can be approximated numerically using Monte Carlo sampling techniques [32]. Here we used a combined approach in which parameter estimates were first obtained by a variational method that approximates these integrals using a saddle point approach to minimize an objective function, providing the maximum likelihood estimate of the distribution. These estimates were then used as starting values in a Monte Carlo algorithm to sample from the full path integral distribution. As with all optimization methods, the variational approach has strengths and weaknesses [64], but it remains a reliable choice for deterministic systems where the derivatives are available [65, 66]. One benefit is that the optimization of state variables, including the data dimension, is performed at every time-point. This allows for

a generic choice of objective function measure, such as least-squares used here (Equation 1), avoiding the question of how to incorporate more subjective measures such as spike number, rise-times, and inter-spike-interval into a meaningful objective function.

A critical concern in variational approaches to nonlinear dynamical systems is that the familiar least-squares objective function may give an irregular search surface with many local minima [67]. We addressed this problem by including a balanced synchronization term, $u(t)(V_{data}(t) - V_m(t))$, in the model dynamics, which regularizes and minimizes the influence of local minima by ensuring that the solution set defines a model that is capable of synchronizing with the data [68–71]. The objective function has a penalty for this regularization and is taken as

$$\frac{1}{T} \sum_{t=1}^T \left\{ (V_{data}(t) - V_m(t))^2 + u(t)^2 \right\}, \quad (1)$$

where $V_{data}(t)$ is the measured voltage, $V_m(t)$ is the voltage output from the model, and T is the number of discretely sampled time points.

The neuron model that we investigated is not known to be chaotic for the biophysical range of our parameters, but it is nonlinear, and in the high dimensional search space there may well exist chaotic regions that must be explored by the optimization routine, and these will benefit from this regularization. We have shown using simulated data that the variational approach using this regularized cost function can recover unmeasured states and parameters, including both maximal conductances and channel kinetics [31, 72].

Provided a solution to the model can be found that is consistent with the data, at the end of the optimization the value for the control parameter $u(t)$, governing the magnitude of the synchronization term, should be small relative to the model dynamics. The quality of the model was tested by setting $u(t)$ to zero and integrating the model forward from the end of the assimilation period using the estimated parameter and state values. The integration algorithm was 4th-order Runge-Kutta with timestep 0.02 ms.

Model Validation

The intra-epoch predictions for completed models were compared to recorded data using five complementary metrics. The correlation coefficient (CC) was the simplest metric, and the most closely related to the objective function used to fit the model. We note that CC strongly penalizes errors in spike timing greater than the width of a spike. The other four metrics required separating the spikes from the subthreshold voltage. Spikes were detected by an algorithm that determined when the voltage crossed a threshold and then located the next peak within 1.5 ms

of the threshold crossing. The time of the peak was considered the spike time. For each spike, the voltage values between 3.5 ms before the peak and 8.0 ms after were extracted to give the spike waveform. The subthreshold voltage was defined by clipping out time points contiguous with the peak of the spike where $V(t) > -50$ mV.

Subthreshold voltage deviance was calculated as the RMS difference between time points in the predicted and measured voltage, excluding points that had been clipped out around spikes in either time series. Spike rate deviance was calculated as $|N_p - N_m| / \max(N_p, N_m)$, where N_p was the number of predicted spikes and N_m the number of measured spikes. Spike shape deviance was calculated by creating a 2-dimensional histogram of the spike waveforms in the phase plane (as in Figure 1E), with one axis corresponding to $V(t)$ and the other to $dV(t)/dt$ [21]. Histograms were bounded between -90 to 60 mV, and -1000 to 1500 mV/ms, with 100 bins in each dimension. The histograms were normalized to a total area of 1.0 and the deviance was the RMS difference between the histograms. Spike timing was compared using the coincidence factor Γ [58], with a window size of 2 ms. This metric compares the number of coincident spikes observed between data and prediction with the number of coincidences expected from a homogeneous Poisson process with the same rate.

When possible, the prediction metrics were also calculated between the assimilation epoch and another epoch with the same stimulus, as a measure of the neurons' intrinsic variability. Not enough neurons were presented with the same stimuli multiple times to enable scores for individual neurons to be corrected for intrinsic variability, but we were able to estimate values for the population. There was a trend for putative RA-projecting neurons to be more precise ($\Gamma = 0.56 \pm 0.06$) than X-projecting neurons ($\Gamma = 0.30 \pm 0.08$), but the difference was not statistically significant (t test, $P = 0.08$).

To choose the best overall model for each neuron, scores on each of the metrics were ranked, with a rank of 1 indicating the lowest deviance, highest correlation, or highest coincidence. Ranks were summed across metrics, and the model with the lowest sum was considered the best overall. CC was used to break ties.

Parameter Uncertainty Calculations

The uncertainty in a solution is dependent upon both measurement and model error, and is expressed by the joint probability distribution resulting from the path integral defined in [31]. This integral can be approximated with numerical sampling, as discussed in detail in [32]. Both measurement and model error were approximated as Gaussian, with measurement error $\sigma_m = 0.4$ mV (obtained experimentally) and model error $\sigma_f = 0.04$ (mV for

V_m , unitless for the gating particles). Using this approximation, we sampled the path distribution

$$P(\mathbf{y}(t)|V_{data}(t)) \propto e^{-A_0(\mathbf{y}(t), V_{data}(t))},$$

with the action, A_0 , given by

$$A_0 = \frac{1}{2T\sigma_m^2} \sum_{t=0}^T (y_1(t) - V_{data}(t))^2 + \frac{1}{2T\sigma_f^2} \sum_{t=0}^{T-1} \sum_{i=1}^{12} \text{TRP}^2(y_i(t), y_i(t+1)), \quad (2)$$

using Metropolis-Hastings Monte Carlo [73, 74]. The model errors are represented in the TRP function, which is the error of the trapezoidal integration rule between the model values at time t and $t+1$. The objective function (Equation 1) used for the variational optimization is clearly reminiscent of the action (Equation 2) but in the limit of vanishing model error where instead the model equations are enforced as constraints. The solution of the variational optimization obtains $u(t) \approx 0$ and represents the maximum likelihood path of this distribution.

Neuron Model

We used a single-compartment, isopotential model with a passive leak conductance and eight active, voltage-gated conductances. We developed the model iteratively, starting with the standard Hodgkin-Huxley transient sodium and non-inactivating potassium channels, along with a nonselective hyperpolarization-activated cation channel (HCN). This model was used in an earlier study with simulated data [31], which showed that the variational method could recover the states and parameters of the model used to simulate data. However, we found that this simple model was unable to reproduce several features of our recordings from real neurons in HVC, so we added additional sodium, potassium, and calcium channels that have been found in a broad range of neurons, some in HVC [75]. In the absence of data on the expression patterns of specific ion channel genes in HVC, we chose relatively wide parameter bounds for the channel kinetic parameters, thereby allowing the currents to represent classes of channels with similar voltage dependence and gating kinetics. The membrane voltage V_m is given by the current conservation equation

$$\frac{dV_m(t)}{dt} = \frac{1}{C_m} (I_{NaT} + I_{NaP} + I_{K1} + I_{K2} + I_{K3} + I_{HCN} + I_{CaL} + I_{CaT} + I_{Leak} + I_{inj}/I_{SA}), \quad (3)$$

where C_m is the specific membrane capacitance, and I_{SA} is a parameter relating to the surface area of the membrane; it sets the scale of the injected current actually seen by the neuron. The I_X are channel currents. Each of the voltage-gated currents depends on ion flow through channels whose permeability is controlled by activation

(m) and inactivation (h) gating variables. $I_{ion}(t) = g_{ion}m(t)^{n1}h(t)^{n2}(E_{reversal} - V_m(t))$, where g_{ion} is a maximal conductance and $n1, n2$ are integers. The voltage-gated currents we included are transient sodium (I_{NaT} ; kinetics m^3h), persistent sodium (I_{NaP} ; m), non-inactivating fast potassium (I_{K1} ; m^4), inactivating potassium (I_{K2} ; m^4h), slow potassium (I_{K3} ; m), hyperpolarization-activated cation (I_{HCN} ; h), high-threshold L-type calcium (I_{CaL} ; m^2h), and low-threshold T-type calcium (I_{CaT} ; m^2).

Each of the sodium, potassium, and leak currents were modeled by the Nernst approximation to the Goldman-Hodgkin-Katz (GHK) current equation, $I_\alpha = g_\alpha X_\alpha (E_{rev} - V_m)$, where g_α is the maximal conductance of the channel, X_α is a channel-dependent and voltage-dependent function related to the proportion of open channels, and E_{rev} is the reversal potential of the active ion species. Due to the large differences in intra- and extracellular calcium concentrations, the full GHK equation was used to describe these currents. For numerical stability, we used a 24th-order polynomial expansion of this equation.

The permeability of each voltage-gated channel species depended on one or more gating variables (e.g. m, h) whose opening and closing was modeled by the Boltzmann barrier-hopping rate,

$$\frac{dm(t)}{dt} = \frac{m_\infty(V_m(t)) - m(t)}{\tau(V_m(t))}, \quad (4)$$

where $m_\infty(V)$ gives the equilibrium activation and $\tau(V)$ gives the time constant as functions of voltage. In terms of the opening rate $\alpha(V)$ and closing rate $\beta(V)$ in the original Hogkin-Huxley formulation [1], $m_\infty = \alpha/(\alpha + \beta)$ and $\tau = 1/(\alpha + \beta)$. These functions are usually expressed in terms of exponentials, but for numerical stability we used a hyperbolic tangent approximation, with

$$\begin{aligned} m_\infty(V_m) &= 0.5(1 + \tanh((V_m(t) - V_{1/2})/\kappa)) \\ \tau(V_m) &= \tau_0 + \tau_{max}(1 - \tanh^2((V_m(t) - V_{1/2})/\sigma)) \\ \frac{dm(t)}{dt} &= \frac{1}{2} \cdot \frac{1 + \tanh((V_m(t) - V_{1/2})/\kappa) - 2m(t)}{\tau_0 + \tau_{max}(1 - \tanh^2((V_m(t) - V_{1/2})/\sigma))} \end{aligned} \quad (5)$$

In this representation, $V_{1/2}$ is the half-activation voltage, κ is the slope of the activation function between the closed and open state, τ_0 is the minimum relaxation time, $\tau_{max} + \tau_0$ is the peak relaxation time, and σ is the width of the relaxation time function. Equations for the inactivation variables (h) have a similar form (see Equation 6). For the K2 and CaT inactivation particles we used a more complex form that allowed relaxation voltage dependence to be asymmetric (see Equation 6 below).

The membrane voltage and the values for each of the gating variables formed a 12-dimensional vector $\{y_1(t), y_2(t), \dots, y_{12}(t)\}$ that described the state of the neuron. The dynamics of the state vector were defined by a set of ordinary differential equations that depended on a number of unknown parameters. The complete set of model equations used for the optimization procedure, including the synchronization-inspired regularization term were as follows:


$$\begin{aligned}
\mathbf{Voltage} : dy_1/dt &= ((p_2 y_2^3 y_3 + p_3 y_4)(p_4 - y_1) + (p_5 y_5^4 + p_6 y_6^4 y_7 + p_7 y_8)(p_8 - y_1) \\
&\quad + (p_{71} y_9^2 + p_{72} y_{10}^2 y_{11}) 19.2970673 (p_{11} - 0.0001 \exp(y_1/13)) / \text{GHK}(y_1) \\
&\quad + p_9 (p_{10} - y_1) + p_{12} y_{12} (-43 - y_1) + I_{inj} / p_{13} / p_1 + u(t) (V_{data}(t) - y_1) \\
\mathbf{NaT}, m : dy_2/dt &= 0.5(1 + \tanh((y_1 - p_{14})/p_{15}) - 2y_2) / (p_{17} + p_{18}(1 - \tanh^2((y_1 - p_{14})/p_{16}))) \\
\mathbf{NaT}, h : dy_3/dt &= 0.5(1 + \tanh((y_1 - p_{19})/p_{20}) - 2y_3) / (p_{22} + p_{23}(1 - \tanh^2((y_1 - p_{19})/p_{21}))) \\
\mathbf{NaP}, m : dy_4/dt &= 0.5(1 + \tanh((y_1 - p_{24})/p_{25}) - 2y_4) / (p_{27} + p_{28}(1 - \tanh^2((y_1 - p_{24})/p_{26}))) \\
\mathbf{K1}, m : dy_5/dt &= 0.5(1 + \tanh((y_1 - p_{29})/p_{30}) - 2y_5) / (p_{32} + p_{33}(1 - \tanh^2((y_1 - p_{29})/p_{31}))) \\
\mathbf{K2}, m : dy_6/dt &= 0.5(1 + \tanh((y_1 - p_{34})/p_{35}) - 2y_6) / (p_{37} + p_{38}(1 - \tanh^2((y_1 - p_{34})/p_{36}))) \\
\mathbf{K2}, h : dy_7/dt &= 0.5(1 + \tanh((y_1 - p_{39})/p_{40}) - 2y_7) / (p_{42} + p_{44} + 0.5(1 - \tanh(y_1 - p_{39})) \\
&\quad \cdot (p_{43}(1 - \tanh^2((y_1 - p_{39})/p_{41})) - p_{44})) \\
\mathbf{K3}, m : dy_8/dt &= 0.5(1 + \tanh((y_1 - p_{45})/p_{46}) - 2y_8) / (p_{48} + p_{49}(1 - \tanh^2((y_1 - p_{45})/p_{47}))) \\
\mathbf{CaT}, m : dy_9/dt &= 0.5(1 + \tanh((y_1 - p_{50})/p_{51}) - 2y_9) / (p_{53} + p_{54}(1 - \tanh^2((y_1 - p_{50})/p_{52}))) \\
\mathbf{CaL}, m : dy_{10}/dt &= 0.5(1 + \tanh((y_1 - p_{55})/p_{56}) - 2y_{10}) / (p_{58} + p_{59}(1 - \tanh^2((y_1 - p_{55})/p_{57}))) \\
\mathbf{CaL}, h : dy_{11}/dt &= 0.5(1 + \tanh((y_1 - p_{60})/p_{61}) - 2y_{11}) / (p_{64} + p_{65}(1 + \tanh((y_1 - p_{60})/p_{62})) \\
&\quad \cdot (1 - \tanh((y_1 - p_{60})/p_{63}))(1 - \tanh(y_1 - p_{60}) \tanh((1/p_{62} + 1/p_{63})(y_1 - p_{60}))) \\
&\quad / (1 + \tanh((y_1 - p_{60})/p_{62}) \tanh((y_1 - p_{60})/p_{63}))) \\
\mathbf{HCN}, h : dy_{12}/dt &= 0.5(1 + \tanh((y_1 - p_{66})/p_{67}) - 2y_{12}) / (p_{69} + p_{70}(1 - \tanh^2((y_1 - p_{66})/p_{68})))
\end{aligned}$$

(6)

Numerical Analysis Details

The optimization was accomplished using the open source software IPOPT [66] and the pardiso [76] or ma57 linear solver libraries, on standard desktop hardware and on a Cray XE6. The data assimilation window over which the model properties were estimated was 1500 milliseconds long; the data were sampled at 50 kHz, resulting in 75,000 time points of voltage data. Common to ‘direct method’ variational approaches, the model trajectories were co-located during the optimization procedure; that is, each component of $\{y_1(t), y_2(t), \dots, y_{12}(t)\}$ was treated as an independent variable with the model dynamical equations imposed as equality constraints between neighboring time-points. Gating particle variables were constrained between 0 and 1, and each of the parameters was constrained between biologically realistic bounds (see Table S1). Data assimilation of the full model took an average of 52 h (range 14–199 h) of computation per epoch on a single core.

The completed model, with estimated parameters and state variables at $t = 1500$ ms, was then integrated forward with $u(t) = 0$ for the remainder of the data epoch with the same injected current that was presented to the real neuron. To generate predictions on different data epochs, a short (100 ms) section of data was used to find the initial conditions for the state variables (the parameters being held fixed at their previously established values), and then the model was integrated forward again with the corresponding injected current and $u(t) = 0$.

The Monte Carlo evaluation of error statistics was performed by a Markov chain that om walks through the space of model variables and parameters. For this calculation, the timeseries of model variables was down-sampled from 50 kHz to 5 kHz, although the entire data assimilation window was used. The initial path was provided by the result of the variational optimization, and the chain was allowed to explore the space about this solution while accepting 5% increases in the objective function with 50% probability. A random perturbation to all variables, $(\mathbf{y}(t), p)$ was considered one step in the Markov chain. The chain was allowed to come to equilibrium over 5×10^6 steps and then 1×10^3 samples were taken, uniformly distributed over the next 2×10^6 steps.

As a technical note, it is essential to fully exercise the ~~dynamical~~ range of the neuron’s dynamics during the data assimilation window [23]. This is achieved by subjecting the neuron to a current with a complicated waveform, exhibiting a broad power spectrum (many characteristic timescales) as well as regions of constant (positive, negative and zero) current to ascertain the neuron’s passive response properties. High frequency currents are not useful as they are filtered out by the RC time constant of the membrane. Our results also indicate that long duration, low frequency currents (including steps) may be essential for uncovering slow potentials like the HCN current. More naturalistic currents may fail to uncover contributions from channels with slower kinetics or smaller maximal conductances, or may require much longer assimilation windows for those contributions to have

a significant influence on the estimated parameters.

References

1. Hodgkin AL, Huxley AF (1952) A quantitative description of membrane current and its application to conduction and excitation in nerve. *J Physiol (Lond)* 117: 500–44.
2. Briggman KL, Abarbanel HDI, Kristan WB (2005) Optical imaging of neuronal populations during decision-making. *Science* 307: 896–901.
3. Marder E, Bucher D (2007) Understanding circuit dynamics using the stomatogastric nervous system of lobsters and crabs. *Annu Rev Physiol* 69: 291–316. doi:10.1146/annurev.physiol.69.031905.161516.
4. Briggman KL, Kristan WB (2008) Multifunctional pattern-generating circuits. *Annu Rev Neurosci* 31: 271–94. doi:10.1146/annurev.neuro.31.060407.125552.
5. Ayali A, Lange AB (2010) Rhythmic behaviour and pattern-generating circuits in the locust: Key concepts and recent updates. *J Insect Physiol* 56: 834–43. doi:10.1016/j.jinsphys.2010.03.015.
6. Hines ML, Carnevale NT (1997) The NEURON simulation environment. *Neural Comput* 9: 1179–1209.
7. Herz AVM, Gollisch T, Machens CK, Jaeger D (2006) Modeling single-neuron dynamics and computations: A balance of detail and abstraction. *Science* 314: 80–85. doi:10.1126/science.1127240.
8. Gleeson P, Crook S, Cannon RC, Hines ML, Billings GO, et al. (2010) NeuroML: A language for describing data driven models of neurons and networks with a high degree of biological detail. *PLoS Comput Biol* 6: e1000815. doi:10.1371/journal.pcbi.1000815.
9. Trimmer J, Rhodes K (2004) Localization of voltage-gated ion channels in mammalian brain. *Annu Rev Physiol* 66: 477–519. doi:10.1146/annurev.physiol.66.032102.113328.
10. Kew JNC, Davies CH, editors (2010) *Ion Channels: From Structure to Function*. New York: Oxford University Press.
11. Schulz DJ, Goillard JM, Marder E (2006) Variable channel expression in identified single and electrically coupled neurons in different animals. *Nat Neurosci* 9: 356–362. doi:10.1038/nn1639.
12. Günay C, Edgerton JR, Jaeger D (2008) Channel density distributions explain spiking variability in the globus pallidus: A combined physiology and computer simulation database approach. *J Neurosci* 28: 7476–91. doi:10.1523/JNEUROSCI.4198-07.2008.

13. Cerda O, Trimmer JS (2010) Analysis and functional implications of phosphorylation of neuronal voltage-gated potassium channels. *Neurosci Lett* 486: 60–7. doi:10.1016/j.neulet.2010.06.064.
14. Johnston J, Forsythe ID, Kopp-Scheinflug C (2010) Going native: Voltage-gated potassium channels controlling neuronal excitability. *J Physiol (Lond)* 588: 3187–3200. doi:10.1113/jphysiol.2010.191973.
15. Golowasch J, Goldman MS, Abbott LF, Marder E (2002) Failure of averaging in the construction of a conductance-based neuron model. *J Neurophysiol* 87: 1129–31.
16. Achard P, Schutter ED (2006) Complex parameter landscape for a complex neuron model. *PLoS Comput Biol* 2: e94. doi:10.1371/journal.pcbi.0020094.
17. Vanier MC, Bower JM (1999) A comparative survey of automated parameter-search methods for compartmental neural models. *J Comput Neurosci* 7: 149–171. doi:10.1023/A:1008972005316.
18. Geit WV, Schutter ED, Achard P (2008) Automated neuron model optimization techniques: A review. *Biol Cybern* 99: 241–251. doi:10.1007/s00422-008-0257-6.
19. Foster WR, Ungar LH, Schwaber JS (1993) Significance of conductances in Hodgkin-Huxley models. *J Neurophysiol* 70: 2502–18.
20. Prinz AA, Billimoria CP, Marder E (2003) Alternative to hand-tuning conductance-based models: Construction and analysis of databases of model neurons. *J Neurophysiol* 90: 3998–4015. doi:10.1152/jn.00641.2003.
21. Druckmann S, Banitt Y, Gidon A, Schürmann F, Markram H, et al. (2007) A novel multiple objective optimization framework for constraining conductance-based neuron models by experimental data. *Front Neurosci* 1: 7–18. doi:10.3389/neuro.01.1.1.001.2007.
22. Reid MS, Brown EA, DeWeerth SP (2007) A parameter-space search algorithm tested on a Hodgkin-Huxley model. *Biol Cybern* 96: 625–634. doi:10.1007/s00422-007-0156-2.
23. Hobbs KH, Hooper SL (2008) Using complicated, wide dynamic range driving to develop models of single neurons in single recording sessions. *J Neurophysiol* 99: 1871–83. doi:10.1152/jn.00032.2008.
24. Buhry L, Pace M, Saighi S (2012) Global parameter estimation of an Hodgkin-Huxley formalism using membrane voltage recordings: Application to neuro-mimetic analog integrated circuits. *Neurocomputing* 81: 75–85. doi:10.1016/j.neucom.2011.11.002.

25. Baldi P, Vanier MC, Bower JM (1998) On the use of Bayesian methods for evaluating compartmental neural models. *J Comput Neurosci* 5: 285–314.
26. Huys QJM, Ahrens MB, Paninski L (2006) Efficient estimation of detailed single-neuron models. *J Neurophysiol* 96: 872–90. doi:10.1152/jn.00079.2006.
27. Huys QJM, Paninski L (2009) Smoothing of, and parameter estimation from, noisy biophysical recordings. *PLoS Comput Biol* 5: e1000379. doi:10.1371/journal.pcbi.1000379.
28. Lepora NF, Overton PG, Gurney K (2011) Efficient fitting of conductance-based model neurons from somatic current clamp. *J Comput Neurosci* doi:10.1007/s10827-011-0331-2.
29. Hendrickson EB, Edgerton JR, Jaeger D (2011) The use of automated parameter searches to improve ion channel kinetics for neural modeling. *J Comput Neurosci* 31: 329–346. doi:10.1007/s10827-010-0312-x.
30. Vavoulis DV, Straub VA, Aston JAD, Feng J (2012) A self-organizing state-space-model approach for parameter estimation in Hodgkin-Huxley-type models of single neurons. *PLoS Comput Biol* 8: e1002401. doi:10.1371/journal.pcbi.1002401.
31. Toth BA, Kostuk M, Meliza CD, Margoliash D, Abarbanel HDI (2011) Dynamical estimation of neuron and network properties I: Variational methods. *Biol Cybern* 105: 217–237. doi:10.1007/s00422-011-0459-1.
32. Kostuk M, Toth BA, Meliza CD, Margoliash D, Abarbanel HDI (2012) Dynamical estimation of neuron and network properties II: Path integral monte carlo methods. *Biol Cybern* 106: 155–67. doi:10.1007/s00422-012-0487-5.
33. Abarbandel HDI (2013) *Predicting the Future: Completing Models of Complex Systems*. New York: Springer.
34. Dutar P, Vu HM, Perkel DJ (1998) Multiple cell types distinguished by physiological, pharmacological, and anatomic properties in nucleus ~~hvc~~ of the adult zebra finch. *J Neurophysiol* 80: 1828–1838.
35. Nixdorf B, Davis S, DeVoogd T (1989) Morphology of Golgi-impregnated neurons in hyperstriatum ventralis, pars caudalis in adult male and female canaries. *J Comp Neurol* 284: 337–349. doi: 10.1002/cne.902840302.

36. Fortune ES, Margoliash D (1995) Parallel pathways and convergence onto HVC and adjacent neostriatum of adult zebra finches (*Taeniopygia guttata*). *J Comp Neurol* 360: 413–441. doi:10.1002/cne.903600305.
37. Kubota M, Taniguchi I (1998) Electrophysiological characteristics of classes of neuron in the HVC of the zebra finch. *J Neurophysiol* 80: 914–923.
38. Shea SD, Koch H, Baleckaitis D, Ramirez JM, Margoliash D (2010) Neuron-specific cholinergic modulation of a forebrain song control nucleus. *J Neurophysiol* 103: 733–745. doi:10.1152/jn.00803.2009.
39. Mooney R (2000) Different subthreshold mechanisms underlie song selectivity in identified HVC neurons of the zebra finch. *J Neurosci* 20: 5420–5436.
40. Mooney R, Prather JF (2005) The HVC microcircuit: the synaptic basis for interactions between song motor and vocal plasticity pathways. *J Neurosci* 25: 1952–1964. doi:10.1523/JNEUROSCI.3726-04.2005.
41. Hahnloser RHR, Kozhevnikov AA, Fee MS (2002) An ultra-sparse code underlies the generation of neural sequences in a songbird. *Nature* 419: 65–70.
42. Jin D, Ramazanoğlu F, Seung H (2007) Intrinsic bursting enhances the robustness of a neural network model of sequence generation by avian brain area HVC. *J Comput Neurosci* 23: 283–299.
43. Roberts TF, Klein ME, Kubke MF, Wild JM, Mooney R (2008) Telencephalic neurons monosynaptically link brainstem and forebrain premotor networks necessary for song. *J Neurosci* 28: 3479–3489. doi:10.1523/JNEUROSCI.0177-08.2008.
44. Long MA, Jin DZ, Fee MS (2010) Support for a synaptic chain model of neuronal sequence generation. *Nature* 468: 394–9. doi:10.1038/nature09514.
45. Daou A, Ross M, Johnson F, Hyson RL, Bertram R (2013) Electrophysiological characterization and computational models of HVC neurons in the zebra finch. *J Neurophysiol* doi:10.1152/jn.00162.2013.
46. Druckmann S, Berger TK, Hill S, Schürmann F, Markram H, et al. (2008) Evaluating automated parameter constraining procedures of neuron models by experimental and surrogate data. *Biol Cybern* 99: 371–9. doi:10.1007/s00422-008-0269-2.
47. Sarkar AX, Christini DJ, Sobie EA (2012) Exploiting mathematical models to illuminate electrophysiological variability between individuals. *J Physiol (Lond)* 590: 2555–67. doi:10.1113/jphysiol.2011.223313.

48. Olypher AV, Calabrese RL (2007) Using constraints on neuronal activity to reveal compensatory changes in neuronal parameters. *J Neurophysiol* 98: 3749–58. doi:10.1152/jn.00842.2007.
49. Bean BP (2007) The action potential in mammalian central neurons. *Nat Rev Neurosci* 8: 451–65. doi:10.1038/nrn2148.
50. Prinz AA, Bucher D, E M (2004) Similar network activity from disparate circuit parameters. *Nat Neurosci* 7: 1345–1352.
51. Swensen AM, Bean BP (2005) Robustness of burst firing in dissociated Purkinje neurons with acute or long-term reductions in sodium conductance. *J Neurosci* 25: 3509–20. doi:10.1523/JNEUROSCI.3929-04.2005.
52. Pospischil M, Toledo-Rodriguez M, Monier C, Piwkowska Z, Bal T, et al. (2008) Minimal Hodgkin-Huxley type models for different classes of cortical and thalamic neurons. *Biol Cybern* 99: 427–41. doi:10.1007/s00422-008-0263-8.
53. Ransdell J, Nair S, Schulz D (2013) Neurons within the same network independently achieve conserved output by differentially balancing variable conductance magnitudes. *J Neurosci* 33: 9950–9956.
54. Tomaiuolo M, Bertram R, Leng G, Tabak J (2012) Models of electrical activity: Calibration and prediction testing on the same cell. *Biophys J* 103: 2021–32. doi:10.1016/j.bpj.2012.09.034.
55. Jolivet R, Lewis TJ, Gerstner W (2004) Generalized integrate-and-fire models of neuronal activity approximate spike trains of a detailed model to a high degree of accuracy. *J Neurophysiol* 92: 959–76. doi:10.1152/jn.00190.2004.
56. Kobayashi R, Tsubo Y, Shinomoto S (2009) Made-to-order spiking neuron model equipped with a multi-timescale adaptive threshold. *Front Comput Neurosci* 3: 9. doi:10.3389/neuro.10.009.2009.
57. Jolivet R, Kobayashi R, Rauch A, Naud R, Shinomoto S, et al. (2008) A benchmark test for a quantitative assessment of simple neuron models. *J Neurosci Methods* 169: 417–24. doi:10.1016/j.jneumeth.2007.11.006.
58. Jolivet R, Schürmann F, Berger TK, Naud R, Gerstner W, et al. (2008) The quantitative single-neuron modeling competition. *Biol Cybern* 99: 417–26. doi:10.1007/s00422-008-0261-x.

59. Jin L, Han Z, Platasa J, Woollorton JR, Cohen LB, et al. (2012) Single action potentials and subthreshold electrical events imaged in neurons with a fluorescent protein voltage probe. *Neuron* 75: 779–785. doi: 10.1016/j.neuron.2012.06.040.
60. Jouvét B, Phythian R (1979) Quantum aspects of classical and statistical fields. *Phys Rev A* 19: 1350-1355.
61. Hochberg D, Molina-París C, Pérez-Mercader J, Visser M (1999) Effective action of stochastic partial differential equations. *Phys Rev E* 60: 6343-6360.
62. Restrepo JM (2008) A path integral method for data assimilation. *Physica D* 237: 14-27.
63. Abarbanel HDI (2009) Effective actions for statistical data assimilation. *Phys Lett A* 373: 4044-4048.
64. Wolpert DH, Macready WG (1997) No free lunch theorems for optimization. *IEEE T Evolut Comput* 1: 67–82.
65. Gill PE, Murray W, Wright MH (1981) *Practical Optimization*. London: Academic Press.
66. Wächter A (2002) *An Interior Point Algorithm for Large-Scale Nonlinear Optimization with Applications in Process Engineering*. Phd thesis, Carnegie Mellon University.
67. Abarbanel HDI, Kostuk M, Whartenby W (2010) Data assimilation with regularized nonlinear instabilities. *Q J Meteor Soc* 136: 769-783.
68. Huijberts HJC, Lilge T, Nijmeijer H (2001) Nonlinear discrete-time synchronization via extended observers. *Int J Bifurcat Chaos* 11: 1997–2006.
69. Abarbanel HDI, Creveling D, Jeanne J (2008) Estimation of parameters in nonlinear systems using balanced synchronization. *Phys Rev E* 77: 016208.
70. Abarbanel HDI, Creveling DR, Farsian R, Kostuk M (2009) Dynamical state and parameter estimation. *SIAM J Appl Dyn Syst* 8: 1341-1381.
71. Szendro IG, Rodríguez MA, López JM (2009) On the problem of data assimilation by means of synchronization. *J Geophys Rev* 114: doi:10.1029/2009JD012411.
72. Abarbanel HDI, Bryant P, Gill PE, Kostuk M, Rofeh J, et al. (2011) Dynamical parameter and state estimation in neuron models. In: Glanzman D, Ding M, editors, *The Dynamic Brain: An Exploration of Neuronal Variability and Its Functional Significance*, New York: Oxford University Press, chapter 8.

73. Metropolis N, Rosenbluth AW, Rosenbluth MN, Teller AH, Teller E (1953) Equation of state calculations by fast computing machines. *J Chem Phys* 21.
74. Hastings WK (1970) Monte Carlo sampling methods using Markov chains and their applications. *Biometrika* 57: 97.
75. Kubota M, Saito N (1991) Sodium- and calcium-dependent conductances of neurones in the zebra finch hyperstriatum ventrale pars caudale in vitro. *J Physiol (Lond)* 440: 131–42.
76. Schenk O, Bollhoefer M, Gärtner K (2008) On large-scale diagonalization techniques for the Anderson model of localization. *SIAM Review* 50: 91–112.

Acknowledgements

B. Toth contributed software used to generate IPOPT code. We acknowledge many productive conversations with P. E. Gill on numerical optimization, and we thank [Arji Daou](#) for conversations about neuron classes in HVC.

Figure Legends

Figure 1. Data assimilation window and prediction window for intracellular responses for exemplar neuron N1. (A) Membrane voltage (top) in response to injection of a complex current waveform (bottom). The black trace shows recorded values, and the cyan trace shows estimated voltage from our data assimilation procedure utilized for time $[0, 1500]$ ms, during which all state variables and parameters of the model were estimated. The magenta trace shows the predicted voltage coming from integrating the model with estimated parameters and state variables forward in time; $t > 1500$ ms. Vertical tick marks indicate times of action potentials. (B) Membrane voltage from a different recording epoch with a different injected current. A brief assimilation period (cyan) (100 ms) using the model from (A) was used to set the initial conditions for the prediction (magenta) in this epoch. (C) Voltage responses (top, black trace) to simple step currents (bottom), with predicted responses from the model in magenta. (D) Detail of randomly selected spikes extracted from the recorded voltage, assimilation estimates, and predictions. (E) The same spikes are plotted in the phase plane to show additional details of the spike shape. Each spike appears as a loop, with increasing time going clockwise. The arrow indicates an initial period of rapid depolarization.

Figure 2. Data assimilation window and prediction of intracellular responses for exemplar N2. The format is the same as in Figure 1. Note the differences with N1 in membrane time constant, lower firing rate, reduced after-spike hyperpolarization, and other aspects of spike shape.

Figure 3. Data assimilation window and prediction of intracellular responses for exemplar N3. The format is the same as in Figure 1. Note the much lower spike rate and strong adaptation compared to N1 and N2.

Figure 4. Estimated ion currents from the completed model for exemplar N1. (A) Voltage response to depolarizing current step. Note the after-spike hyperpolarization, consistent spike height, and minimal adaptation. (B) Currents from the major fast sodium and potassium channels from the model. Only the fast sodium (NaT) and inactivating potassium (K2) currents contribute significantly to spike generation. (C) Estimated values for the Na activation (solid blue line) and inactivation (dashed blue line) gating variables, and the K2 activation and inactivation gating variables (cyan lines). The full range from 0 to 1 is shown. (D–F) Details of voltage, current, and gating variable estimates for the indicated spike in (A–C).

Figure 5. Estimated ion currents from the completed model for exemplar N2. The format is the same as in Figure 4. Similar to N1, only the fast sodium (NaT) and inactivating potassium (K2) currents contribute significantly to spike generation, but note the relatively stronger NaT vs K2 current and the buildup of inactivation during long depolarizations that leads to spike rate and shape adaptation.

Figure 6. Estimated ion currents from the completed model for exemplar N3. The format is the same as in Figure 4. Differing from N1 and N2, the slow, non-inactivating potassium (K3) current drives repolarization and remains open during prolonged depolarization. Also note the slight presence of the NaP current between spikes.

Figure 7. Comparison of currents and channel kinetics for exemplar neurons. (A) Maximal conductances (\tilde{g} , dark bars) and average currents (\tilde{I} , light bars) relative to the total conductance or average current for each of the major currents in the model, for neurons N1 (blue), N2 (green) and N3 (red). I_{HCN} is not shown as it did not contribute significantly to any of the models. (B) Kinetics of the activation and inactivation variables for NaT, K2, and K3 channels for the exemplar neurons, shown in terms of their equilibrium activation $x_\infty(V)$ and relaxation time $\tau(V)$.

Figure 8. Posterior distributions of selected parameters. The uncertainty in the reported parameter solution set for the membrane capacitance C_m and maximal conductances of neurons N1 (blue), N2 (green) and N3 (red). Using a Metropolis-Hastings Monte Carlo algorithm, the distribution was sampled with the variational method estimates for initial guesses.

Figure 9. Comparison of simple and complex model prediction quality. Each panel shows one of the metrics of how well models predicted various features of the intracellular voltage trace. Points connected by lines correspond to individual neurons and show the values for the best model in each class. For deviance metrics, smaller values indicate closer agreement with recorded data, whereas for correlation coefficient, larger values indicate better agreement. Blue, green, and red dots correspond to exemplar neurons. Red dots displaced to either side indicate median values, and vertical bars the 25th and 75th percentiles. The 9-current model is significantly better for all metrics (paired Wilcoxon test: all $P < 0.008$).

Figure 10. Distributions of selected parameters for 22 HVC neurons. (A) Estimated relative maximal conductances (\tilde{g}) for each of the currents in the model separated by the putative neuron class (RAn: projects to RA; Xn: projects to area X). Permeabilities for the calcium channels were converted to conductances by evaluating the GHK expression with the estimated calcium concentrations. Black points, indicating individual neurons, are horizontally jittered for clarity. Red points and error bars indicate means and 95% confidence intervals (estimated by bootstrapping). Light blue, green, and red dots correspond to exemplar neurons. Asterisks indicate significant difference between putative neuron classes (Wilcoxon test, $P < 0.05$). Total K conductance (K_{total}) is the sum of \tilde{g} for K1–3. (B) Kinetic parameters for activation (left) and inactivation (right) of the NaT channel. $V_{1/2}$, half-activation; κ , the slope of the equilibrium state; σ , the width of the relaxation time function; τ_{max} , the peak time constant. The ranges of the plot ordinates correspond to the upper and lower bounds for the parameters.

Table 1. Prediction quality metrics for models of 26 HVC neurons. Multiple models for each neuron were estimated with data from different recording epochs. The left columns show summary statistics for all the models; the central columns show statistics for all the models, and the right columns show statistics comparing measured responses to the same stimulus. IQR: interquartile range.

Metric	All Models ^(a)				Best Models ^(b)		Intrinsic	
	median	IQR ^(c)	σ_{neuron} ^(d)	σ_{epoch} ^(e)	median	IQR	median	IQR
subthreshold deviance (mV)	3.5	2.3–5.3	5.4	4.8	2.6	1.7–3.8	5.9	4.2–6.8
spike rate deviance	0.22	0.049–0.38	0.27	0.24	0.09	0.00–0.26	0.12	0.09–0.21
spike shape deviance	0.087	0.070–0.13	0.041	0.042	0.077	0.060–0.096	0.064	0.049–0.092
spike coincidence (Γ)	0.38	0.25–0.57	0.29	0.23	0.45	0.32–0.69	0.54	0.38–0.63
correlation coefficient	0.87	0.80–0.92	0.21	0.10	0.88	0.84–0.92	0.87	0.83–0.92

(a) statistics for all neurons and epochs

(b) statistics for best models for each neuron

(c) interquartile range (i.e., 25th and 75th percentile)

(d) sample standard deviation between neurons

(e) sample standard deviation between epochs from the same neuron

Supporting Information

Table S1. The complete list of optimization bounds and model parameter estimates for exemplar neurons N1–N3.

Figure S1. Prediction quality metrics for models estimated with different sets of data from the exemplar neurons N1–N3.